Dynamics and spectra of a solvated electron in water clusters

R. N. Barnett and Uzi Landman
School of Physics, Georgia Institute of Technology, Atlanta, Georgia 30332

Abraham Nitzan
School of Chemistry, Tel Aviv University, Tel Aviv 69978, Israel

(Received 24 March 1988; accepted 13 May 1988)

The dynamics and spectra of negatively charged water clusters, containing a single excess electron, are investigated. In our calculations the atomic water constituents of the clusters are treated classically while the excess electron is described quantum mechanically using the fast Fourier transform algorithm to solve the Schrödinger equation. Information about ground and excited electronic states corresponding to the equilibrium, finite temperature, ground-state ensemble configurations can be obtained by solving for these states for given nuclear configurations generated via quantum mechanical path-integral molecular dynamics simulations. As an alternative, more efficient way, we introduce the adiabatic simulation method which consists of propagating the nuclei in real time while concurrently annealing the electronic wave functions to their correct values corresponding to the instantaneous, dynamically generated nuclear configurations. The resulting trajectories can be used for analyzing nuclear motion in the ground electronic state as well as for calculating energy distributions for the ground and excited electronic states and the (vertical) excitation line shape. We study the cluster size effect on these quantities, and in particular, by comparing results for $(H_2O)_{64}^-$ and $(H_2O)_{128}^-$, we conclude that the vertical ionization potential increases while the vertical excitation energy to the bound excited state decreases for larger cluster sizes. For the smallest negatively charged water cluster $(H_2O)_2^-$, where adiabatic separation of electronic and nuclear motion does not hold, we simulate the time evolution in the TDSCF approximation. The dynamics reveals the close correlation between the electronic binding energy and the cluster dipole, and provides information on intramolecular and intermolecular vibrational motion. Comparison of vibrational density of states evaluated from the nuclear trajectories of the negatively charged and the neutral dimer shows that most of the modes associated with intermolecular motions shift to the red upon electron attachment (a few modes, possibly those associated directly with the magnitude of the total molecular dipole, shift to the blue).

I. INTRODUCTION

Significant advances have been made recently in theoretical investigations of electron localization in ionic[1] and polar[2–4] clusters, electron solvation in molten ionic salts,[5,6] polar liquids[7–12] and rare-gas fluids,[13,14] and in studies of quantum liquids[15] and adsorption systems.[16] Much of the progress in these areas has been achieved via the development of computer simulation methods which allow treatment of the quantum aspects inherent to these systems. These methods include the quantum Monte Carlo (QMC) method,[17] quantum path-integral Monte Carlo (QPIMC),[18] and quantum path-integral molecular dynamics (QUPID) simulations,[5,18,19] which rest upon the Feynman path-integral formulation of quantum statistical mechanics[20] and the recently developed generalized molecular dynamics (GMD)[21] based on the density functional formalism. In the context of electron solvation, recent path-integral based simulations[1–5,7–14,18] provided most valuable insights about the ground-state thermal equilibrium energetics, structure, stability, and excess electron localization modes in small clusters and bulk liquid systems, as well as cluster isomerization processes induced by electron attachment.[1]

While the quantum simulation methods mentioned above open new avenues for investigations of the ground-state and thermal equilibrium properties of many systems of interest, they are not ideally suited for studies of real-time dynamical processes. Nevertheless, recent progress toward this goal, which may prove to be of practical value, has been made.[22–25] An alternative approach is based on direct investigation of the time-dependent Schrödinger equation. In this context, the development of the fast Fourier transform (FFT) algorithm for integrating the time-dependent Schrödinger equation[26,27] has led to several demonstrations of the usefulness of this approach for solving quantum dynamical problems involving small (one to four degrees of freedom) quantum systems.[28] Since, in this method, the computational effort increases exponentially with the number of degrees of freedom, approximate methods have to be used for larger systems. Among those, the time-dependent self-consistent-field (TDSCF) method[29–31] emerges as an important tool due to its efficiency and the ease with which it can be generalized and adapted to different complex situations. In particular, the TDSCF approximation can be easily adapted for the description of a quantum subsystem coupled to a classical one,[31–33] in a scheme which conserves the quantum

 0021-9606/88/162242-15$02.10

mechanical average of the total energy as well as other constants of the motion. Consequently, the method can be used in studies of the dynamics of solvation of quantum particles in a medium of classical molecules.

In this paper, which extends a preliminary report,[33] we discuss and demonstrate several modes of applications of the FFT algorithm and the TDSCF method. In these investigations we focus on the attachment of a single excess electron to small clusters, in particular water clusters. In addition to demonstrating the feasibility and utility of the different modes of calculation we provide new information on electron localization and solvation in small clusters, thus supplementing the equilibrium results obtained previously via QUPID simulations.[1,2] The main results of our studies may be summarized as follows:.

(1) Excited-state energies of the solvated electron are obtained as functions of the cluster size. Most easily obtained are vertical transition energies for transitions in which the cluster configuration remains unchanged. Adiabatic transition energies (where the electronic transition is accompanied by cluster reorganization) may also be obtained, in principle, using a more complicated procedure. Moreover, unbound resonance states of the excess electron may also be identified. The vertical excitation energies may be averaged over ground-state cluster configurations (sampled from an equilibrium ensemble) to yield the absorption line shape. In this case, the availability of equilibrium configurations obtained from quantum mechanical path-integral simulations is useful. Indeed such a procedure has been employed most recently in calculations of the optical absorption spectra of an electron solvated in bulk liquid water[8] and of an excess electron in fluid helium.[13(a)] Alternatively, the adiabatic simulation method described below may be used efficiently for calculations of the absorption spectra.

(2) Ground- and excited-state wave functions for the solvated electron in water clusters are obtained via an imaginary time implementation of the FFT method. The same procedure may also be used to verify results obtained for ground-state and equilibrium clusters from the QUPID method.[2(c)]

(3) The full dynamics of the negative ion cluster can be followed within the TDSCF approximation. The TDSCF time evolution of the $(H_2O)_2^-$ ion is used to demonstrate this mode of simulation. The results illustrate the dynamical correlation between the molecular motions and the excess electron binding and the effect of electron attachment on the vibrational spectrum of the host cluster.

(4) A combination of real and imaginary time implementations of the FFT method is introduced[33] and used in a novel way to follow the adiabatic, ground-state dynamics (GSD), of $NaCl^-$ and negatively charged water clusters. In this adiabatic simulation method (ASM), the electron is restricted, by repeated use of imaginary time evolution, to the ground state corresponding to the instantaneous nuclear configuration generated by real-time evolution of the nuclear motions on the self-consistently calculated electronic ground-state potential energy surface. As will be discussed, this method affords a significant reduction in computational time for processes which are essentially adiabatic as compared to the full dynamical evolution, and is not necessarily limited to the electronic ground state. The calculated estimate for the excess electron absorption bandwidth are in close agreement with the experimental result for a solvated electron in water.

In what follows we first briefly review the FFT algorithm for solving the time-dependent Schrödinger equation and its use in conjunction with the TDSCF approximation. Next we use the FFT method, for fixed nuclear configurations, generated via path-integral simulations, to obtain information about ground, excited, and resonance states for water clusters of various sizes and for the NaCl negative ion. The ground-state energies are compared to those obtained previously by QUPID simulations. Subsequently, the adiabatic simulation method (ASM) is introduced and used for evaluation of the ground-state dynamics and excitation spectra of negatively charged water and NaCl clusters. Finally, the TDSCF dynamics of the negatively charged water dimer is evaluated and discussed. The interatomic interaction potentials and those between the excess electron and the atomic constituents of the clusters employed in these studies are the same as those described and used in previous QUPID simulations.[2]

II. METHOD

For a system described by the Hamiltonian $\hat{H} = \hat{K} + \hat{V}$, where $\hat{K}$ and $\hat{V}$ are the kinetic and potential energy operators, the time evolution of the wave function $\psi(\mathbf{r},t)$ can be performed by second-order differencing[27] or by repeated application of the split (for small time increments, Δt) exponential time-evolution operator[26]

$$\begin{aligned}\psi(\mathbf{r},t+\Delta t) &= e^{-(i/\hbar)(\hat{K}+\hat{V})\Delta t}\psi(r,t) \\ &= e^{-(1/2)(i/\hbar)\hat{K}\Delta t}e^{-(i/\hbar)\hat{V}\Delta t} \\ &\quad \times e^{-(1/2)(i/\hbar)\hat{K}\Delta t}\psi(\mathbf{r},t)+O(\Delta t^3). \quad (1)\end{aligned}$$

While both iteration methods are of the same formal accuracy [the error is of order $(\Delta t)^3$], the exponential evolution is, in our experience, more stable and therefore allows the use of a bigger time step (Δt). Another advantage of the exponential method is that real and imaginary time evolutions can be performed on equal footing, while second-order time differencing diverges for imaginary time and thus first- (with corresponding loss of accuracy) or third-order differencing have to be used. (We note however that differencing techniques have their own advantages, in particular for multiconfiguration TDSCF computations.)

The fast Fourier transform (FFT) algorithm for the evaluation of Eq. (1) is based on the fact that the kinetic energy operator $[\hat{K} = -(\hbar^2/2m)\nabla^2]$ is diagonal in the momentum representation and thus expansion in a plane wave, free particle, basis set yields

$$\begin{aligned}\psi(\mathbf{r},t+\Delta t) &= \frac{1}{(2\pi)^3}e^{-(i/2\hbar)\hat{K}\Delta t}e^{-(i/\hbar)V(\mathbf{r})\Delta t} \\ &\quad \times \int d^3k\, e^{-i\mathbf{k}\cdot\mathbf{r}}e^{-(i\hbar k^2/4m)\Delta t}\int d^3r'\, e^{i\mathbf{k}\cdot\mathbf{r}'}\psi(\mathbf{r}',t). \quad (2)\end{aligned}$$

The Fourier transformations in the above equation are per-

formed using the efficient FFT algorithm. Implementation of the FFT procedure requires that the wave function $\psi(\mathbf{r},t)$ be defined on a grid, with periodic boundary conditions. This is the main limitation of the method when applied to small (one to four) quantum degrees of freedom. For larger systems the method is further constrained mainly by computer memory size requirements, and even with the largest available vector machines one has to resort to approximations in order to treat more than two quantum particles.

In the TDSCF Hartree approximation[30] the wave function for a system of N coupled quantum particles is written as a product:

$$\Psi(\mathbf{r}_1,...,\mathbf{r}_N;t) = \prod_i \phi_i(\mathbf{r}_i,t)e^{-i\eta(t)}, \tag{3}$$

where the single particle wave functions $\phi_i(\mathbf{r},t)$ satisfy the equations of motion

$$i\hbar\dot{\phi}_j = H_j\phi_j + \langle V(\{\mathbf{r}\})\rangle_j\phi_j \quad (j=1,...,N), \tag{4}$$

where a dot represents differentiation with respect to time, $H_j(\mathbf{r}_j)$ is the single particle Hamiltonian for particle j, and where $V(\{\mathbf{r}\})$ is the interparticle interaction. $\langle V(\{\mathbf{r}\})\rangle_j$ denotes the quantum-mechanical expectation value of V over all coordinates except $\mathbf{r}_j$. The phase η is given by

$$\dot{\eta} = \langle\psi|V(\{\mathbf{r}\})|\psi\rangle. \tag{5}$$

Using this approximation leads to significant saving of computing effort. While there is no systematic way to estimate the accuracy of this approximation, there is a growing base of evidence, including comparisons to exact results, supporting the adequacy of the approximation in many situations. Failure of TDSCF procedures may often be traced to using a wrong set of coordinates (to be made separable by the approximation) or to situations where multiple configurations have to be explicitly taken into account. Various remedies are being developed for such circumstances.[28,34–37]

A further simplification which leads to additional saving in computing effort is to limit the quantum dynamical description to a small subsystem, while describing the dynamics of the rest of the system by classical (or sometimes semiclassical) mechanics. The equations of motion for such mixed quantum-classical systems are given by

$$i\hbar\dot{\psi}(\mathbf{r}_Q;\mathbf{r}_C,t) = H_Q(\mathbf{r}_C)\psi(\mathbf{r}_Q;\mathbf{r}_C,t), \tag{6a}$$

$$H_Q(\mathbf{r}_C) = K_Q + V(\mathbf{r}_Q,\mathbf{r}_C), \tag{6b}$$

$$m_C\ddot{\mathbf{r}}_C = -\left\langle\frac{\partial V(\mathbf{r}_Q,\mathbf{r}_C)}{\partial\mathbf{r}_C}\right\rangle - \frac{\partial U(\mathbf{r}_c)}{\partial\mathbf{r}_c}, \tag{6c}$$

where $\mathbf{r}_Q$ and $\mathbf{r}_C$ denote collectively the sets of quantum and classical coordinates, respectively, U is the interaction potential between the classical constituents of the system, and $\langle V\rangle$ is the expectation value of the quantum-classical coupling potential taken with the instantaneous quantum wave function.

An appealing feature of the mixed quantum-classical TDSCF description is that it makes it possible to include temperature in the simulation.[6,33,38–40] This is done by imposing thermal equilibration on the classical part of the system in one of several possible ways. In the present work (as in previous QUPID simulations[1,2,4]) this was done by occasionally randomizing the velocities of randomly chosen classical particles according to an appropriate Maxwellian distribution.[41]

As mentioned above the FFT algorithm is a grid method which implies the existence of limitations on the spatial and temporal resolution that it can achieve, as well as on the extent of the energy range that it can describe.[26–28] For our present applications a matter for concern is the presence of (roughly speaking) two length scales in the problem: (a) a long distance scale associated with the Coulomb and polarization (attractive) interactions and (b) a short range repulsion between the excess electron and the molecular electron charge distribution, originating from the exchange and exclusion terms in the interaction potential. This raises the potential problem of having to use computationally prohibitive large grids in order to accommodate both length scales. In order to test this issue we have applied the FFT algorithm for the solution of the one-dimensional time-dependent Schrödinger equation for a particle moving in a model potential composed of a short range repulsive part and a long range attractive component. The potential is defined by

$$V(r) = \begin{cases} e^{-B(r-\rho)} - e^{-B(R_0-\rho)}; & r\leqslant R_0 = 2^{1/6}A \\ 4\epsilon\left[\left(\frac{A}{r}\right)^2 - \left(\frac{A}{r}\right)^6\right] + \epsilon; & r\geqslant R_0 \end{cases} \tag{7}$$

with $A = B = \epsilon = 1$, $\rho = 3.5$. These values are chosen such that the potential is continuous. The Fourier transforms of the time correlation functions $\langle\psi(0)\psi(t)\rangle$ for grids of 16 and 64 points are shown in Fig. 1. The positions of peaks on this plot correspond to the eigenvalue spectrum of the problem.[26] It is evident that little difference is found in comparing the results obtained with the two different size grids. The origin of this apparent insensitivity to grid size lies in the fact that at least for low lying states the wave functions do not appreciably occupy the regions of strong repulsion, and therefore the error incurred due to the low resolution of their description in these regions is rather small. It will be seen below that good agreement between our results and those

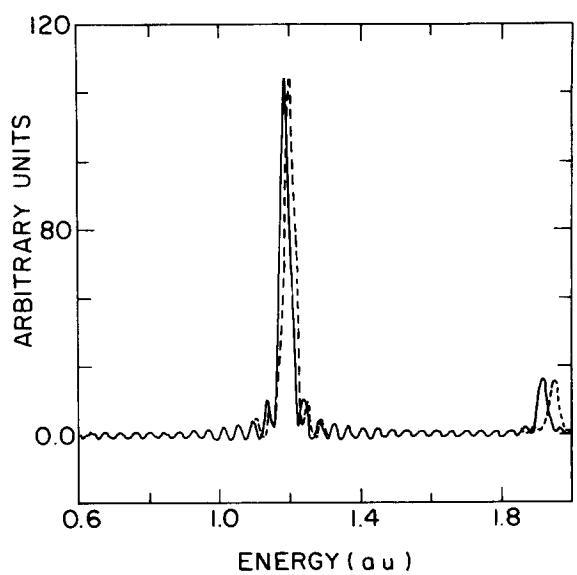

FIG. 1. Fourier spectra (transforms of the time correlation function) $\langle\psi(0)\psi(t)\rangle$ for motion of a quantum particle in a model potential [Eq. (7)]. The solid and dashed lines correspond to 16 and 64 point grids (for the same length of calculational cell), respectively.

obtained via QUPID simulations for the ground-state properties of excess electrons in water clusters is achieved in calculations employing $16\times16\times16$ grids, and an appropriate size of the calculational cell.

Having made this observation, the FFT algorithm can be used as a powerful and fast method to obtain ground- and excited-state information for the excess electron for given static cluster configurations. In such calculations (which do not involve the TDSCF approximation) the cluster configuration is given as a static structure and the quantum problem becomes that of solving the (three-dimensional) single particle Schrödinger equation in a given potential. One can proceed along one of the following ways:

(a) Start with an arbitrary initial wave function and integrate the time-dependent Schrödinger equation using appropriate time increments as required by the energy scale of interest and for a long enough time as implied by the required energy resolution. Using the resulting wave function at time t, $\psi(t)$, form the correlation function $C(t)\equiv\langle\psi(0)\psi(t)\rangle$ and Fourier transform it with respect to time, i.e., $I(E)=\int C(t)\exp(-iEt/h)dt$. The peak positions in the resulting function of energy $I(E)$ correspond to the energy levels of the electron in the given potential. (Obviously only eigenvalues corresponding to eigenfunctions which are not orthogonal to the chosen initial wave function will be obtained in this way. This method can be therefore used to map eigenvalues corresponding to different symmetries by choosing appropriate initial states.) As seen below, this procedure, originally used by Feit *et al.*,[26] yields not only bound-state energies but can also be used to obtain the energies associated with resonance states.

(b) Start with an arbitrary initial wave function and integrate the time-dependent Schrödinger equation in imaginary time $t=-i\beta'$ from $\beta'=0$ to a value β large enough so that the expectation value $E=\langle\psi(\beta)H\psi(\beta)\rangle/\langle\psi(\beta)\psi(\beta)\rangle$ converges to a constant value. The resulting value of E is the ground-state energy, and the corresponding $\psi(\beta)$ is the ground-state wave function, unless the initially chosen wave function $\psi(0)$ is orthogonal to the ground state.[42,43] In general this procedure will lead to the state of lowest energy for any given initial symmetry.

(c) The procedure described in (b) may also be used[43] to obtain excited-state energies and wave functions after the lower states have been found by projecting out lower (previously found) states during the (imaginary) time evolution.

In the context of our present problem, i.e., electron solvation, the information obtained by either one of these methods corresponds to vertical transitions in which the cluster molecular configuration is frozen during the electronic transition. A comprehensive analysis of the excess electron spectrum[8] can be made by using an ensemble of equilibrium cluster configurations generated by QUPID simulations as input for calculations of the spectra using the FFT technique (see Sec. IV).

III. THE ADIABATIC SIMULATION METHOD (ASM)

When the system is composed of two subsystems whose dynamics are characterized by widely separated time scales, we encounter a situation which is normally treated within the adiabatic or Born–Oppenheimer approximation. In this case we also expect the TDSCF approximation, where the total wave function is taken to be separable in the two subsystems, to work well. However, this apparently favorable situation poses difficulties in numerical studies as in any system involving widely separated time scales. In this section we introduce and apply a new numerical method which exploits this time scale separation and is optimally suited for numerical simulations. In fact, by construction, the method is a numerical implementation of the adiabatic approximation where the dynamics of the slow subsystem is followed while the fast subsystem is constrained to stay in one state (which changes adiabatically as the slow subsystem evolves in time). This restriction is implemented by a repeated application of the time evolution operation in imaginary time to the wave function of the fast subsystem followed by appropriate (numerical) projection operators.

We illustrate the method for a system consisting of an electron and several (classical) molecules. Consider the motion of the classical subsystem when the electron is in its ground state. We note first that the vertical excitation energy of an electron in, say, $(H_2O)_{64}^-$ is ~2 eV which is much larger than both kT at room temperature and the characteristic vibrational energies of water. Consequently, the electron excitation energy and the nuclear kinetic energy are well separated and the adiabatic approximation is valid. For any given nuclear configuration the ground electronic state may be found by the imaginary time evolution procedure as described in Sec. II. The adiabatic simulation method (for ground-state dynamics) proceeds from this configuration via the following steps:

(1) Integrate the (Newton) equations of motion for the classical subsystem [Eq. (6c)], keeping the electronic wave function frozen, for a time interval Δt.

(2) Subsequent to the nuclear motion, the electron is not in its exact ground state as was the case prior to that motion. At this stage the electron is quenched to its ground state by the quantum-mechanical imaginary-time evolution operator, while keeping the nuclei fixed in their instantaneous (new) positions. No elapsed real time is counted for this stage.

(3) Now that the electron is in its ground state for the new nuclear configuration, classical time evolution is performed for another Δt interval [step (1)] and the process repeats.

This sequence of real-time evolution of the slow (in this case classical) subsystem, followed by quenching of the wave function using imaginary-time evolution in the fast quantum system, constitutes the adiabatic simulation method (ASM). In most applications this procedure will be applied in the ground electronic state (ground-state dynamics, GSD). To carry out the same procedure for any other electronic state, the imaginary-time relaxation (quenching) should be done in conjunction with projecting out all lower energy states as described in Sec. II.

An example of the adiabatic time evolution in the $(NaCl)^-$ negative ion is shown in Fig. 2. In this calculation, the interaction between the Na^+ and Cl^- ions, the pseudo-

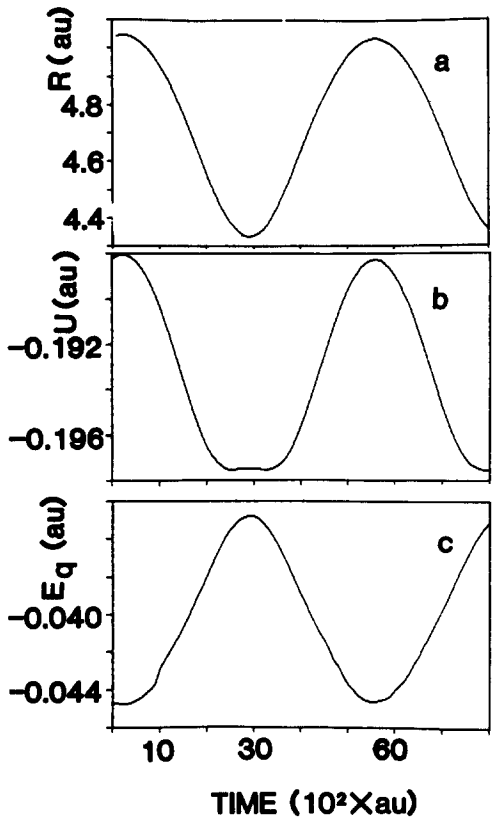

FIG. 2. Dynamics of the internuclear distance (R), interionic potential energy (U), and energy of the electron (E_q), (a), (b), and (c), respectively, for $NaCl^-$ at 50 K. Distance in a.u. $= 1\ a_0 = 0.529\ 17$ Å, energy in a.u. $= 27.2108$ eV, and time in units of the atomic time unit $= 2.4189\times10^{-17}$ s.

potential describing the interaction between the excess electron and the alkali cation and the repulsive interaction with the negative chlorine anion are the same as those discussed previously.[1,44] For this system the ground and excited electronic state are well separated as is seen from the eigenstate spectrum shown in Fig. 3, in which we display the Fourier transform $I(E)$ of $\langle\psi(0)|\psi(t)\rangle$ obtained for a static nuclear configuration at the equilibrium distance $R_{\text{Cl-Na}} = 4.74\,a_0$ of the $(NaCl)^-$ anion. It is evident that in the equilibrium configuration the electronic ground state is ~ 1 eV (0.04 a.u.) below the ionization threshold ($E = 0$) (in agreement with

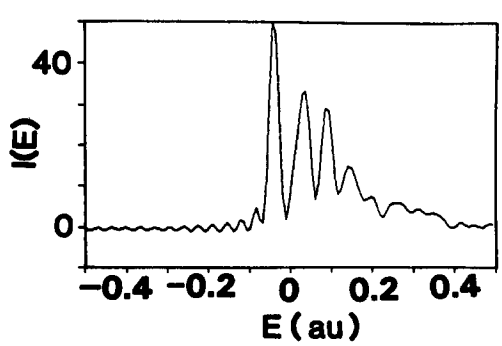

FIG. 3. Fourier transform spectra (in arbitrary units) of the time correlation function $\langle\psi(0)\psi(t)\rangle$ for $NaCl^-$ showing a bound state at ≈ -0.04 a.u. and several resonances.

previous QUPID calculation[44]), that no other bound excited states exist and that the first resonance state is at ~ 0.8 eV (0.03 a.u.) above zero. Since in this system the variation in the separation between the ground electronic state and all other electronic states remains large relative to the nuclear vibrational kinetic energy the application of the adiabatic simulation method for a study of the dynamics of this system is justified. In Fig. 2 we show the time variation of the interionic distance (R), interionic potential energy (U), and of the electron binding energy (E_q), vs time, obtained by an adiabatic simulation of the system at 50 K. We observe that the oscillations in the excess electron binding energy (E_q) occur with the same frequency at which the nuclei oscillate and that E_q achieves its (negative) extremum for the largest internuclear separation (R) [compare Figs. 2(a) and 2(c)]. The frequency of the nuclear vibrational motion of $(NaCl)^-$ obtained via this GSD simulation is $0.75\times10^{13}\ s^{-1}$ in good agreement with the measured[45] value of $0.794\times10^{13}\ s^{-1}$. Comparison to the vibrational frequency of NaCl ($1.094\times10^{13}\ s^{-1}$)[46] shows that the weakening of the interionic bond due to the attachment of an excess electron results in a softening of the vibrational motion.

The manner in which the ASM is carried out in the present study is tantamount to a classical molecular dynamics simulation of the nuclear motion on a potential energy surface which is evaluated concurrently quantum mechanically. It is thus reminiscent of the recent work of Parrinello and Car[21] (although that work was limited to equilibrium simulations it can be extended to include nuclear classical dynamics). More recently a TDSCF simulation (employing the FFT algorithm) of an electron solvated in bulk molten sodium chloride was performed.[6] As discussed by these authors,[6] the dynamics in this system is adiabatic and this simulation is therefore similar in nature to the one which we discussed, though the ASM technique which we described exploits the adiabatic nature of the electronic motion resulting in an improved efficiency of the calculation.

Before concluding this section we mention a technical point concerning ASM simulations. Since the step involving quenching of the electronic wave function to the ground state (or any other selected state) involves a decrease in energy, a closed system (i.e., thermally isolated), followed in this manner, will exhibit monotonous cooling in time. When the adiabatic approximation holds, this cooling rate is very small and can be neglected for all practical purposes for trajectories of reasonable duration. However, in principle, this effect may limit the length of the calculated trajectories. In all the applications of the method reported in this paper, problems related to this issue do not arise since our simulations are performed at constant temperature.

In the following sections we focus on the energetics and dynamics of an excess electron solvated in water clusters. In these studies we employ the various modes of simulations discussed above to determine ground- and excited-state properties and dynamical characteristics of solvated electron in water clusters of different sizes. In addition we compare the ground-state properties obtained via our calculations with previous results obtained via equilibrium path-integral molecular dynamics (QUPID) simulations.[2]

IV. GROUND AND EXCITED ELECTRONIC STATES OF $(H_2O)_n^-$ CLUSTERS: STATIC CONFIGURATIONS

The discoveries of nonreactive electron attachment of electrons to small clusters of water[47–49] and ammonia[50] add a new dimension to the research of electron solvation in polar fluids and of the general issues of size effects on chemical and physical phenomena, pertaining to the questions of the modes of electron localization and the minimal cluster sizes which sustain bound states of an excess electron.[1,2,4,51] Recent theoretical investigations using the path-integral molecular dynamics (QUPID) method[2,4] elucidated the microscopic energetics and mechanisms which underlie electron localization in these systems and the dependence of the localization modes (surface and interior states) on the cluster size and chemical constituents. These calculations employed intermolecular interactions which provide an adequate description of water[52] and ammonia,[53] and a newly developed electron–molecule pseudopotential[2] constructed in the spirit of the density functional theory and consisting of Coulomb, polarization, exclusion, and exchange interactions. The main findings of these investigations may be summarized as follows:

(1) The localization mode of an excess electron in a polar molecular cluster depends on the cluster size and chemical constituents. For water clusters $(H_2O)_n^-$ in the size range $11 \leqslant n < 64$ the electron is relatively strongly bound in a surface state while for larger clusters a transition to internal solvation occurs. Attachment of the excess electron to small clusters, $n < 10$ is in a diffuse weakly bound surface state.

(2) The onset of stable well-bound electron attachment to ammonia clusters $(NH_3)_n^-$ occurs via internal localization, requiring $n \gtrsim 32$ molecules, and in contrast to the case of the water clusters is *not* preceded by well-bound surface states for smaller clusters.[4] The critical sizes for electron binding to water and ammonia clusters are in agreement with experimental observations.[47–50]

(3) The mechanism underlying the mode of localization (surface vs internal states) is a balance between the excess electron binding energy to the cluster and the energy associated with structural molecular reorganization in the cluster upon electron attachment. In the small and medium size water cluster regime ($n < 64$) and for all sizes of ammonia clusters the cluster reorganization energy associated with the formation of an internal electron state is large compared to that which is gained via binding, resulting in surface localization of the excess electron. The transition to internal localization is associated with a reversal of the balance between binding and reorganization energies.

(4) The vertical binding energies calculated via the QUPID simulations[2] for $(H_2O)_n^-$ clusters in the range $12 \leqslant n \leqslant 18$ are in good agreement with those available from photoelectron spectroscopy experiments.[49]

(5) The smallest water cluster which binds an electron is the dimer $[(H_2O)_2^-]$. The binding occurs at low temperature ($T < 20$ K), in a weak-binding (~ 3 meV) diffuse state.[2,3,54]

At this stage it is valuable to compare results obtained by using the methods described in this paper with those obtained for the equilibrium ground state via QUPID simulations, and provide additional information (which is not accessible by other methods) about the excited-state spectra and real-time dynamics of negatively charged clusters.

Results obtained for the equilibrium ground-state energies of $(H_2O)_n^-$ cluster by QUPID simulations and by using the FFT algorithm averaged over randomly selected cluster configurations taken from the QUPID generated equilibrium ensembles,[2(c)] are summarized in Table I. Shown are the electron potential $\langle V \rangle$ and kinetic $\langle K_q \rangle$ energies, their sum $\langle E_q \rangle$, which is the vertical binding energy of the electron, and the radii of gyration of the electron distribution R_g. For the temperatures at which the QUPID simulations were performed ($T = 20$ K for $n = 2$, 79 K for $n = 8$, 12, and 18, and 300 K for $n = 32$, 64, and 128), kT is low relative to the vertical transition between the lowest binding state and the first excited state (except for the dimer where the two quantities are comparable) thus assuring that the QUPID results

TABLE I. Ground-state energies calculated via the FFT and QUPID methods, for $(H_2O)_n^-$ clusters. $\langle V \rangle$, $\langle K_q \rangle$, and $\langle E_q \rangle$ are the electron potential, kinetic, and total quantum binding energies, respectively, in hartrees. $\langle R_g \rangle$ is the electron-distribution radius of gyration in a_0. Temperatures in the QUPID calculations were: $n = 2$ at 20 K; $n = 8$, 12, 18 at 70 K; $n = 32$, 64, 128 at 300 K. For $n = 2$, 8, 12 the electron attachment is via a surface state. For $n = 18$ both the surface (S) and bulk (B) states are given {the former possesses a higher adiabatic electron affinity [Refs. 2(b) and 2(c)]}. For $n = 32$, 64, 128—bulk states. The FFT results are averaged over several arbitrarily selected equilibrium configurations taken from the QUPID simulations. For $n = 2$ the molecular configurations were chosen to be those which are similar to those found for the neutral cluster. Note that except for $n = 2$ the quantum energy $\langle E_q \rangle$ corresponds to the ground-state energy $\langle E_g \rangle$ of Sec. V.

$(H_2O)_n^-$	$\langle V \rangle$	$\langle K_q \rangle$	$\langle E_q \rangle$	$\langle R_g \rangle$
$n = 2$	−0.000 83	0.000 67	−0.000 16	56
QUPID	−0.000 8	0.000 7	−0.000 1	38
$n = 8$	−0.021 6	0.013 7	−0.007 8	11.7
QUPID	−0.021 2	0.013 7	−0.007 4	11
$n = 12$	−0.066 6	0.034 4	−0.032 3	6.9
QUPID	−0.074 5	0.038 2	−0.036 3	6
$n = 18S$	−0.083 9	0.046 2	−0.037 7	5.9
QUPID	−0.092 0	0.043 8	−0.048 2	5.5
$n = 18B$	−0.148 6	0.078 1	−0.070 5	4.2
QUPID	−0.154 3	0.082 3	−0.072 0	4.1
$n = 32$	−0.166 7	0.085 9	−0.080 8	4.0
QUPID	−0.177 8	0.086 9	−0.090 8	3.8
$n = 64$	−0.193 0	0.086 5	−0.106 5	4.0
QUPID	−0.204 2	0.086 6	−0.117 6	3.8
$n = 128$	−0.214 6	0.085 2	−0.129 4	4.0
QUPID	−0.216 9	0.086 5	−0.130 4	3.9

may be safely associated with the ground electronic state. The ground-state energies and wave functions for selected cluster configurations were obtained by the method of evolution in imaginary time described in Sec. II, with the nuclei held at fixed positions. Therefore, the values so obtained correspond to the cluster configuration taken. Thus, although for the $(H_2O)_{18}^-$ cluster binding in an interior state is stronger than in a surface state, this does not indicate that the interior localization is favorable, since the mode of localization is determined by the total energy balance of the cluster (i.e., the adiabatic binding energy, which in addition to the electron vertical binding energy includes the cluster reorganization energy). As evident from Table I, the values obtained by the two methods are in good agreement with each other. The differences are within their corresponding limits of uncertainty.

In addition to the ground state, the FFT calculations (with imaginary-time evolution) can be used to obtain excited state energies and wave functions by requiring that the wave function be orthogonal to wave functions corresponding to lower energies as described in Sec. II. We use the $(H_2O)_{64}^-$ cluster to demonstrate the results. For this system the values obtained for the three lowest excited states (averaged over the same randomly chosen equilibrium configurations as in Table I) are $\langle E_q \rangle = -0.84$, -0.45, and -0.29 eV and the corresponding widths $[R_g = (\langle r^2 \rangle - \langle r \rangle^2)^{1/2}]$ are 6.0, 8.1, and 8.6 a_0 (where a_0 is the Bohr radius). These results were obtained using a limited number of cluster configurations. The corresponding values obtained for the excited states of the $(H_2O)_{128}^-$ cluster are: -1.31, -0.92, and -0.65 and for R_g, 5.5, 5.6, and 5.9 a_0. More accurate results for the lowest excited state obtained via the adiabatic simulation method which effectively averages over many configurations are presented in Sec. V. Examples of contour plots of the ground- and excited-state excess electron distributions obtained for a randomly chosen cluster configuration of $(H_2O)_{64}^-$ are shown in Fig. 4. The ground-state distribution shown in Figs. 4(a) and 4(b) has s-like character while those for the three lowest excited states [Figs. 4(c), 4(e), and 4(f)] are p-like [the three-dimensional plot corresponding to Fig. 4(c) is shown in Fig. 4(d)]. Note, however, that the marked deviations from spherical symmetry of the molecular environment of the excess electron are reflected in the splitting of the excited-state energy levels and in the shapes of the corresponding electron distributions (see also Ref. 8). For aid in visualization we show in Figs. 5(a) and 5(b) three-dimensional images of a typical water cluster configuration and electron densities for the ground and excited states in $(H_2O)_{64}^-$, respectively. In these figures the electron density $|\psi|^2$ is represented by randomly distributing dots in a given volume element, using the spatial distribution $|\psi(\mathbf{r})|^2$ as a weight function.

An alternative way[26] for calculating ground- and excited-state energies of a given static nuclear configuration is, as described in Sec. II, to evolve $\psi(t)$ in real time from a given, arbitrary wave function $\psi(0)$ and to compute the Fourier transform of the correlation function $\langle \psi(0) | \psi(t) \rangle$. Examples of Fourier spectra obtained in this manner for four $(H_2O)_{64}^-$ cluster configurations are shown in Fig. 6, demonstrating the existence of bound ground and excited states. In addition, the variations in the locations of the peaks (corresponding to the excess electron energy levels) for different cluster configurations [Figs. 6(a)–6(d)] illustrate their dependence on the structural fluctuation of the host cluster. Similar calculations for smaller negatively charged $(H_2O)_n^-$ clusters show that the onset of a bound excited state in these clusters occurs in the size range $32 \lesssim n < 64$.

In order to extract from such calculations reliable state distributions and spectroscopic data, extensive averaging over cluster configurations is necessary. This was indeed done recently for an electron solvated in the bulk water[8] and in fluid helium.[9] In Sec. V we present results of ground-state dynamics (GSD) simulations for $(H_2O)_{64}^-$ and $(H_2O)_{128}^-$ which achieve the same goal in a more efficient manner, providing, in addition, information about the nuclear dynamics in these systems.

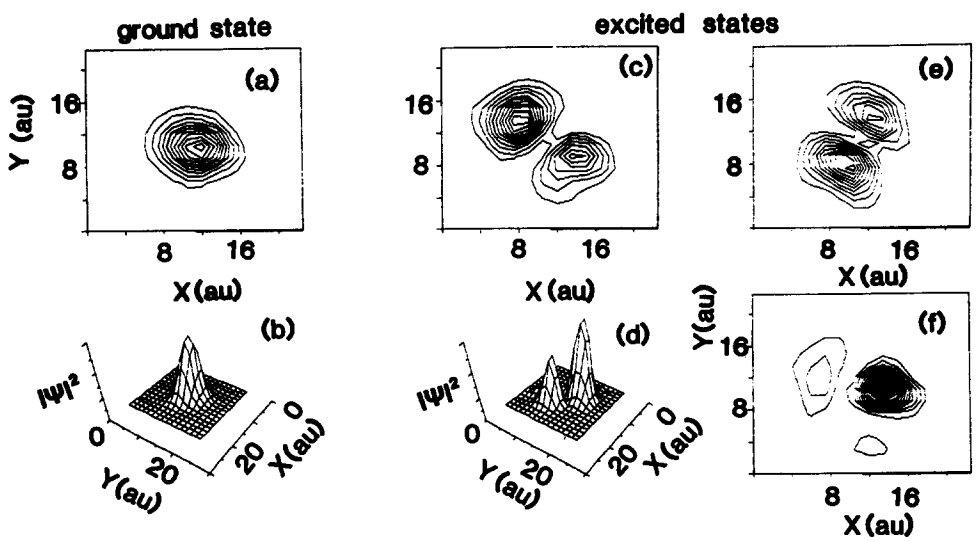

FIG. 4. Two- and three-dimensional contours of the excess electron density in the ground [(a) and (b)] and three lowest excited states [(c)–(f)] in the $(H_2O)_{64}^-$ cluster. The three-dimensional contour in (d) corresponds to the two-dimensional one shown in (c). Note the p character of the excited states. All contours are calculated in the xy plane at the middle of the z axis of the calculational cell. Distances are in atomic units.

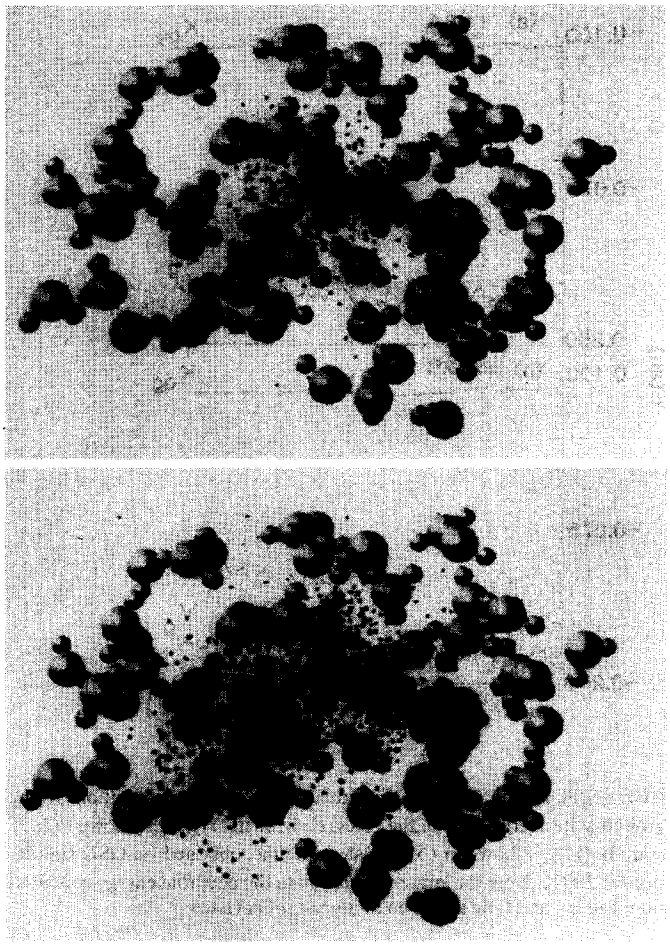

FIG. 5. Images of a typical molecular configuration (large and small balls) corresponding to oxygens and hydrogens, respectively, and excess electron distribution (small dots) in $(H_2O)_{64}^-$, obtained via an FFT solution to the three-dimensional Schrödinger equation. Note the diffuseness of the excited-state electron distribution [shown in (b)] compared to the relatively compact nature in the ground state [shown in (a)]. The molecular cluster configuration was randomly chosen from QUIPD simulations [Ref. 2(c)].

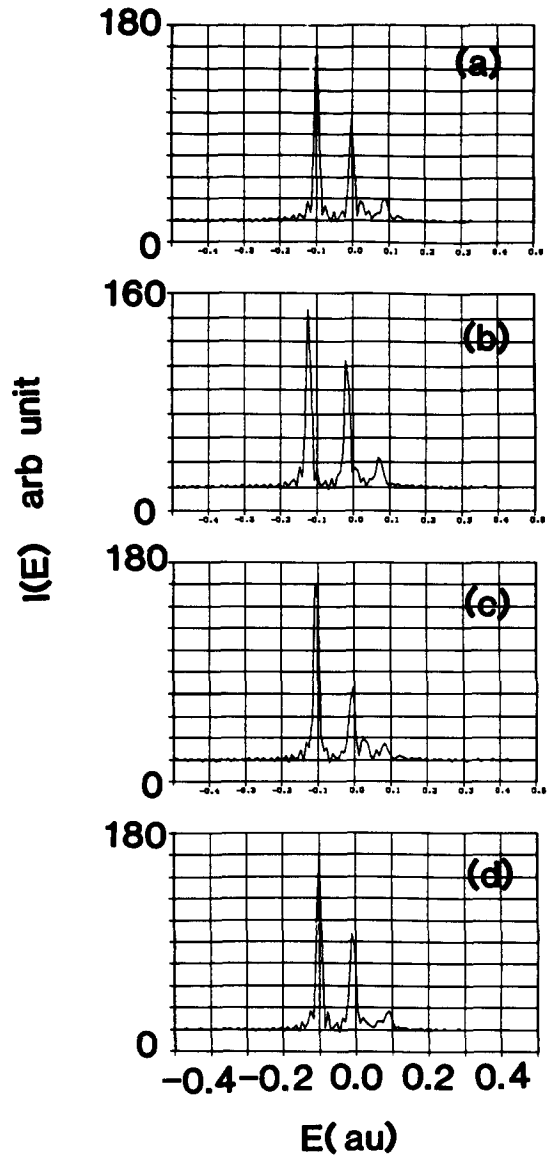

FIG. 6. Fourier spectra of the time correlation function $\langle\psi(0)\psi(t)\rangle$ detailed via the FFT method, for four randomly chosen cluster configurations of $(H_2O)_{64}^-$ obtained via QUPID simulations [Ref. 2(c)] at 300 K. The variations in the peak positions, corresponding to the energy levels of the excess electron, demonstrate their dependence on the cluster molecular configuration. Note that the peak corresponding to the excited state contains the three unresolved (for the short trajectory used in this calculation) p-like energy levels shown in Fig. 4. Energy in atomic units.

V. GROUND-STATE DYNAMICS (GSD) OF NEGATIVELY CHARGED WATER CLUSTERS

The ground-state dynamics (GSD) method [or more generally the adiabatic simulation method (ASM)] where the classical nuclear dynamics evolves on the adiabatic electronic potential energy surface (the adiabatic ground-state surface in the GSD method) calculated quantum mechanically for the time-dependent nuclear configurations, was described in Sec. III. In Figs. 7–9 we present results of such simulations for $(H_2O)_{64}^-$ and $(H_2O)_{128}^-$ clusters at 300 K, which support both ground and excited bound electronic states. As discussed by Schnitker *et al.*,[8] and in Sec. IV, the lowest excited levels are three closely spaced p-type orbitals (see Fig. 4), that would have been degenerate if spherical symmetry applied. The results presented below pertaining to the ground state and lowest excited state were obtained from a simulation in which typically the classical dynamics was followed for 2×10^3 time steps ($\Delta t = 10$ a.u. $= 2.4\times10^{-16}$ s). Every classical time step is followed by a quench to the ground- and excited-state wave functions in the new nuclear configuration. In the quench stage the wave functions are evolved in imaginary time while keeping the excited-state wave function orthogonal to that of the ground state. A typical imaginary time step used in this process was $\Delta t = -i\Delta\beta = -0.5i$ a.u. (where $i=\sqrt{-1}$). Using $\Delta t = -1.0i$ did not result in significant differences. For the ground- and excited-state quenches we have used 10 and 20 such steps, respectively, after each classical step. To check that this quench time span was sufficient (particularly for the excited state, i.e., that the quench of the wave function to the lowest excited state was complete and that the two other close lying excited states were annealed out) we performed test simulations for the $(H_2O)_{64}^-$ clusters in which a longer

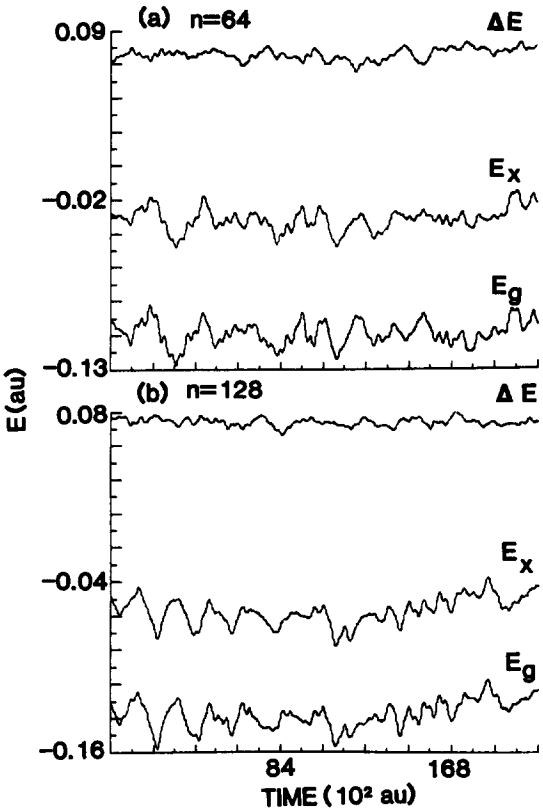

FIG. 7. Excess electron energies of the ground (E_g) and excited (E_x) states and their difference (ΔE) vs time, obtained via ground-state dynamics (GSD) simulations of $(H_2O)_n^-$ clusters with $n = 64$ [shown in (a)] and $n = 128$ [shown in (b)]. The simulations were performed at 300 K. Note the stronger binding of the excess electron in the larger cluster, and that the fluctuation in E_x and E_g occur largely in-phase resulting in relatively smaller fluctuations of their difference (ΔE). Energy and time in atomic units (a.u.).

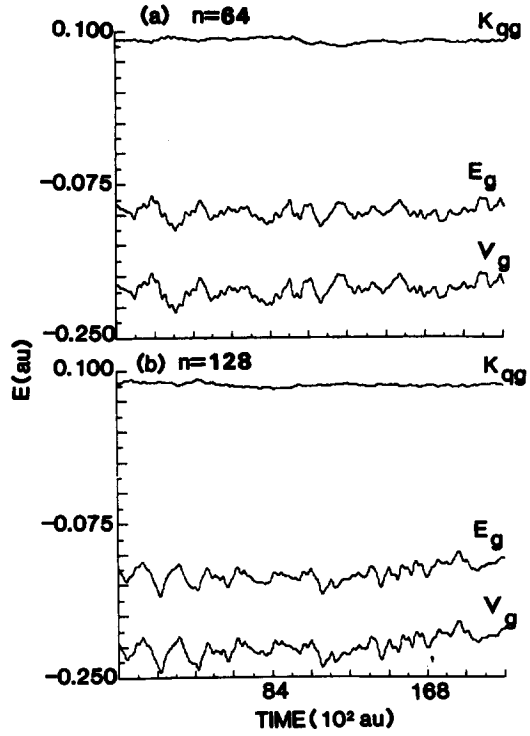

FIG. 8. The kinetic (K_{gg}) and potential (V_g) energy contributions to the ground-state energy (E_g) of the excess electron in $(H_2O)_{\bar{64}}$ [shown in (a)] and $(H_2O)_{\bar{128}}$ [shown in (b)] clusters vs time, obtained via GSD simulations at 300 K. Note the larger fluctuation in the potential energy contribution. Energy and time are given in atomic units (a.u.).

quench time span was used for both the ground- and excited-state wave functions.

The spatial grid used in these simulations consists of 16^3 points in a cube with a linear dimension $L = 24\,a_0$. Doubling the number of points along each direction (i.e., 32^3 point grid) for fixed L did not affect the results in any significant manner. Throughout the simulations the center and width of the electronic wave functions were monitored to assure that their spatial extent remains well within the calculational grid. The computational time required for the generation of a 2×10^3 classical time step trajectory was $\sim$7.5 CPU hours for $(H_2O)_{\bar{64}}$ and 15 CPU hours for $(H_2O)_{\bar{128}}$ on a CDC CYBER 990 computer. For the $(H_2O)_{\bar{64}}$ cluster, several trajectories were generated starting from different initial conditions. All these yielded similar results thus indicating that trajectories calculated for this time span (2000 classical steps with $\Delta t = 10$ a.u.) perform an adequate sampling of the accessible phase space resulting in good statistical distributions and averages. Finally, both constant energy and constant temperature ($T = 300$ K) simulations were performed yielding results with no significant difference when $E = \langle E \rangle$, where E is the constant energy in the constant energy simulation and $\langle E \rangle$ the time averaged total energy in the constant temperature one.

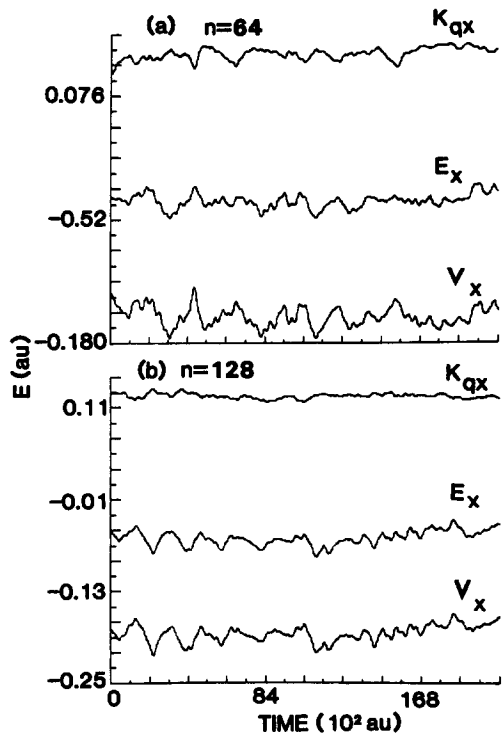

FIG. 9. Same as Fig. 8 for the kinetic (K_{qx}) and potential (V_x) contribution to the first excited-state energy (E_x).

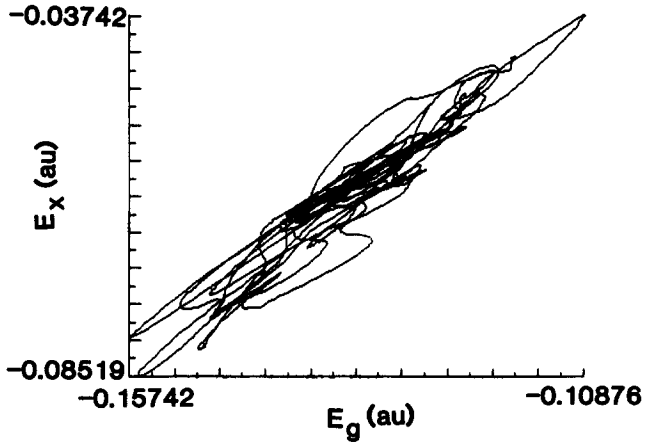

FIG. 10. Correlation diagram for the first excited-state energy (E_x) vs the ground-state energy (E_g) for the $(H_2O)_{64}^-$ cluster, obtained via GSD simulations. The strong correlation and approximate linear relationship between the two energies is evident.

The energies of the electronic ground and excited states and their difference vs time are shown in Figs. 7(a) and 7(b) for $(H_2O)_{64}^-$ and $(H_2O)_{128}^-$, respectively. In Figs. 8(a) and 8(b) we display the time evolution of the kinetic and potential energy contributions to the total electronic ground-state energy for $(H_2O)_{64}^-$ and $(H_2O)_{128}^-$, respectively. Similar data for the lowest excited state are shown in Figs. 9(a) and 9(b).

The stronger electron binding in the $(H_2O)_{128}^-$ cluster relative to that in $(H_2O)_{64}^-$ is evident from Fig. 7. Figure 7 also shows that fluctuations in the ground (E_g)- and excited (E_x)-state energies occur largely in phase, so that fluctuation in their difference ΔE are considerably small. Another way to demonstrate the correlated variations in E_g and E_x is to plot them against each other, as shown in Fig. 10 for the $(H_2O)_{128}^-$ cluster. From this figure we deduce that on the average E_g and E_x are linearly related.

Figures 8 and 9 show pronounced fluctuations in the instantaneous electron energies. Note, however, that the fluctuation in the quantum kinetic energy K_q are of smaller amplitude than those of the potential energy contribution E_p, particularly in the ground state (Fig. 8). This implies (as expected) that the electronic wave function is less sensitive to the dynamical changes in the cluster configuration than the interaction potential energy of the electron with the cluster.

The mean ground and first excited-state energies $\langle E_g \rangle$ and $\langle E_x \rangle$ and the corresponding standard deviations σ_g and σ_x ($\sigma = \sqrt{\langle E^2 \rangle - \langle E \rangle^2}$) obtained from the GSD trajectories for $(H_2O)_n^-$, $n = 32, 64, 128$ are summarized in Table II. For $(H_2O)_{32}^-$ no reliable excited-state data could be obtained since the lowest excited state lies very close to the ionization threshold ($E = 0$) which made convergence to it prohibitively slow. The $\langle E_g \rangle$ results presented here are more accurate than those presented in Table I since many more configurations (the full GSD trajectory) are involved in the averaging process. Nevertheless, the results in Table I ($\langle E_q \rangle$ values) compare favorably with those given in Table II.

The fluctuations in the electronic energy difference ΔE

TABLE II. Mean ground ($\langle E_g \rangle$)- and excited ($\langle E_x \rangle$)-state energies of the excess electron and the mean excitation energies $\langle \Delta E \rangle = \langle E_x \rangle - \langle E_g \rangle$ for $(H_2O)_n^-$ clusters at 300 K, calculated via ground-state dynamics simulations. σ_g, σ_x, and $\sigma_{\Delta E}$ are the variances of the corresponding quantities. Energies are given in units of hartree (a.u.). The values of $\langle E_g \rangle$ correspond to the equilibrium quantum energy E_q in Table I.

$(H_2O)_n^-$	$\langle E_g \rangle$	σ_g	$\langle E_x \rangle$	σ_x	$\langle \Delta E \rangle$	$\sigma_{\Delta E}$
$n = 32$	−0.0784	0.0084				
$n = 64$	−0.1073	0.0074	−0.0334	0.0069	0.0745	0.0034
$n = 128$	−0.1339	0.0094	−0.0612	0.0094	0.0727	0.0027

(see Fig. 7) induced by the nuclear motions are the origin of the broad absorption spectrum characteristic to the hydrated electron. Such spectroscopic information can be obtained via ensemble averaging or equivalently via a single time trajectory of sufficient time span to assure that the accessible phase space is sampled adequately. The latter method was used in our study. Accordingly, long records of the time evolution of the ground and excited states obtained via a GSD simulation (see Fig. 7) are used in order to construct histograms of the number (frequency) of occurrences of different values of E_g, E_x, and ΔE vs energy. As mentioned, care has been taken that the time span of the simulation was long enough to achieve adequate (convergent) sampling of the accessible phase space (i.e., effective equilibrium ensemble averaging). Such histograms (obtained from the data in Fig. 7) showing the distributions of E_g, E_x, and ΔE are displayed in Figs. 11 and 12 for $(H_2O)_{64}^-$ and $(H_2O)_{128}^-$, respectively. We remark that the absorption line shape corresponds to the ΔE distribution weighted by the squared transition-dipole matrix element $|\mu_{gx}|^2$ between the two electron states. We have found that this correction to line shapes, given in Figs. 11(c) and 12(c), is very small. Several features displayed in Figs. 11 and 12 should be noticed. First the broad energy distributions in the ground- and excited-state energies are an indication of the large sensitivity of the electronic energy to the cluster configurations. As noted above this sensitivity is due mostly to the potential energy terms. The fact that the broadening is due more to fluctuations in the interaction potential rather than to changes in the wave function is probably the reason for the somewhat narrower distributions associated with the excited-state energies.

Second, noted above, the fact that E_g and E_x fluctuate largely in unison is the origin of the substantially narrower distribution of the gap energy (ΔE). ΔE is seen to peak at ~ 0.075 hartree ($\simeq 2.04$ eV) for $(H_2O)_{64}^-$ with a small shift to the red for $(H_2O)_{128}^-$. For an electron in bulk water the peak of the absorption band is at 1.73 eV.

Finally, the widths of the ΔE distributions, Figs. 11(c) and 12(c), are of the order of 0.01 hartree = 0.27 eV. The experimentally observed width in bulk water is 0.8 eV. This larger width reflects the fact that three nondegenerate p states contribute to the line shape while in the above GSD simulation we evaluated only the lowest of them for each

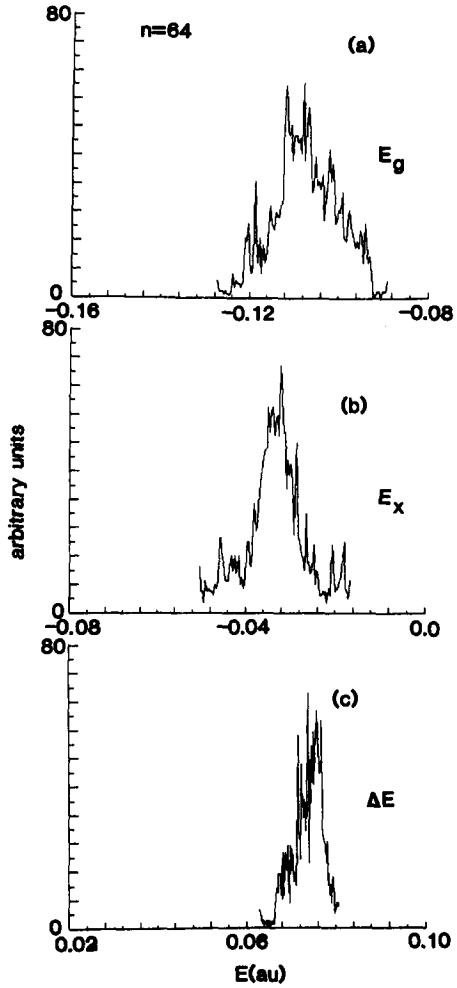

FIG. 11. Histograms of the frequency of occurrence of different energy values, obtained from GSD simulations of $(H_2O)_{64}^-$ at 300 K for the ground (E_g)- and excited (E_x)-state energies and the difference between them (ΔE). The breadth of the energy distributions correspond to the widths of the energy levels and that of ΔE corresponds to the width of the absorption spectrum for the ground to first excited-state transition. The broadening of the levels is due to time fluctuations (at finite temperature) in the cluster molecular configuration. The mean values of these energy distributions are given in Table II. Energy is given in atomic units.

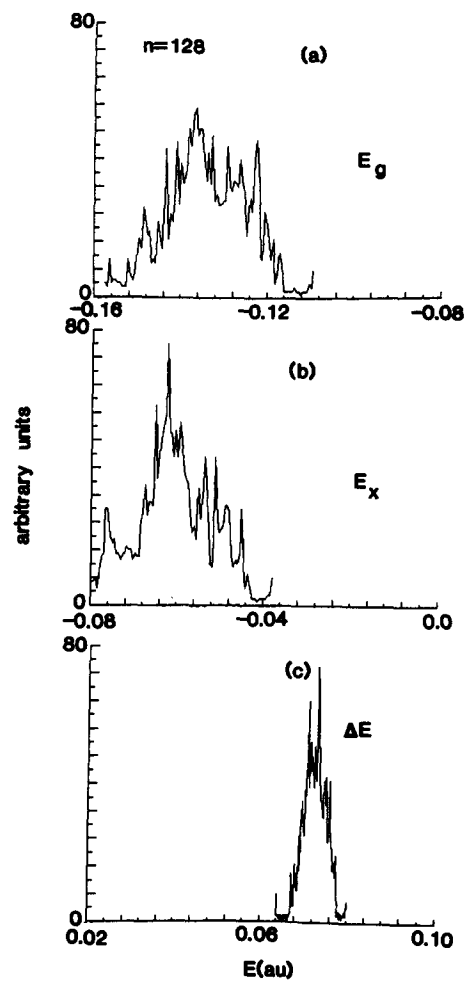

FIG. 12. Same as Fig. 11 for $(H_2O)_{128}^-$ at 300 K. The mean values of E_g, E_x, and ΔE are given in Table II.

configuration. Indeed, having observed (Sec. IV) that the three lowest p-like excited states span an energy range of $\sim$0.5–0.7 eV, and assuming that the width (of 0.27 eV) is the same for all of them the theoretical estimate of the absorption bandwidth comes close to the experimental one.[55] [The small differences observed in our calculations of the bandwidth results for the $(H_2O)_{64}^-$ and $(H_2O)_{128}^-$ clusters suggest that finite size effects on these widths are small in this cluster size range justifying the comparison to the bulk water data.] We note that the calculation of Schnitker *et al.*[8] overestimates this width by $\sim$40%. The difference between their results and ours are probably due to the different potentials used for the description of the intra- and intermolecular interactions in water, the electron–water interaction.

To conclude this section we note that the results of Fig. 8 provide an *a posteriority* justification for the use of the adiabatic simulation method by showing that the energy separation between the ground and excited states in these systems remains always large relative to the nuclear energies. In Sec. VI we consider an extreme case where this separation of energies does not hold and where full dynamical simulation (in the TDSCF approximation) has to be performed.

VI. TDSCF DYNAMICS OF $(H_2O)_2^-$

The water dimer is the smallest water cluster known to attach an electron, with an estimated[2(a),3,54] binding energy in the range of 3–25 MeV (depending on the molecular configuration of the dimer[2(a)]) which is of the same order as the energy of the lowest intermolecular vibrational mode of the neutral dimer.[52] Since an adiabatic separation of the electronic and nuclear motions cannot be assumed here, the ASM computational scheme cannot be used. Instead we have simulated the full dynamical evolution of the $(H_2O)_2^-$ in the TDSCF approximation, under the added assumption that the water molecular motions can be treated, as before, classically.

With regard to the first approximation we should note that the structure of the negatively charged water dimer (Fig. 13), with a very diffuse electron charge density weakly

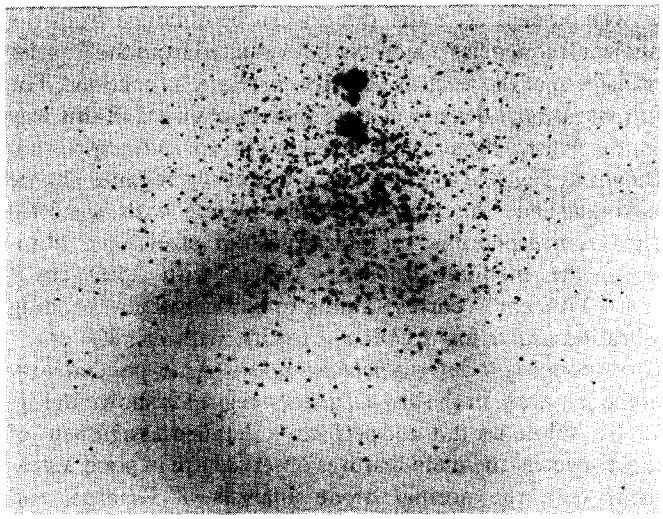

FIG. 13. Image of a typical low-dipole configuration generated in a TDSCF dynamical simulation at 20 K of the $(H_2O)_2^-$ cluster (large and small balls correspond to oxygens and hydrogens, respectively) and of the excess electron charge distribution (small dots). We note that this molecular configuration is very similar to that of the neutral dimer. Note the diffuseness of the electron distribution.

bound to the water dimer via primarily dipolar interactions, supports the assertion that the TDSCF approximation may be used in this situation. Separation of the electronic and nuclear motions may be achieved here not because they evolve on different time scales but because they occur on different length scales.

Figure 14 shows, for $(H_2O)_2^-$ at $T=20$ K, the time evolution of several quantities: the classical potential energy U, the total classical energy E_{cl}, the kinetic (K_q) potential (V) and total (E_q) quantum energies of the electron (V is of course the energy of interaction between the electron and the classical system), the spatial spread of the electron charge distribution $[R_g = (\langle r^2\rangle - \langle r\rangle^2)^{1/2}]$, and the total dipole of the water molecular dimer. In this calculation we used a 16^3 grid with grid unit equal to 9 a_0, and have monitored the position and width of the electron wave packet to make sure that it remains well within the calculational grid throughout the evolution.[56] We remark that such a large grid cell is appropriate for the description of the very diffuse, weakly bound, electronic wave function. The time length of the trajectory shown is 8×10^4 a.u. $\cong 2$ ps.

The results in Fig. 14 clearly exhibit the correlation between the nuclear motion and the electronic energies. In particular the strong effect of the total cluster dipole on the electron binding energy is evident. The electronic energy fluctuates between values very close to zero and values below -8×10^{-4} hartree (~ -22 MeV) as the structure of the cluster alternates between high- and low-dipole configurations. The existence of such configurations of the negatively charged water dimer at 20 K was already demonstrated by the QUPID simulations.[2(a)] Inspection of Fig. 14 shows that the transition time between the high- and low-dipole configurations is roughly in the range 0.1–1 ps.

From the time records of the total interaction potential energy (U), Fig. 14(a), between the atomic constituents of

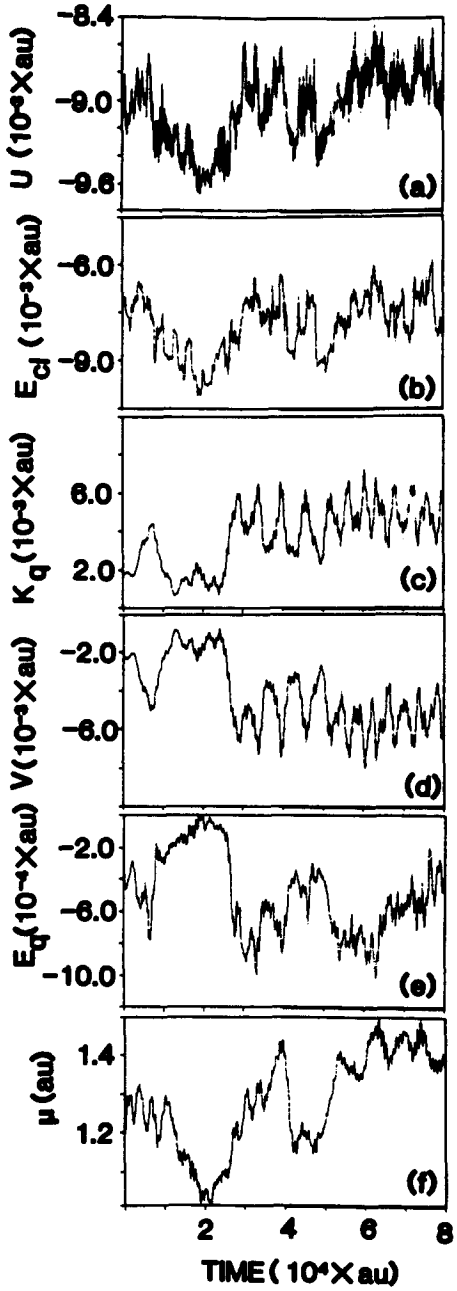

FIG. 14. Results obtained from TDSCF dynamical simulations of $(H_2O)_2^-$. The molecular potential energy (U), total classical energy (E_{cl}), kinetic energy of the excess electron (K_q), interaction energy between the excess electron and the molecular cluster (V), total energy of the excess electron (E_q), and total dipole moment of the water molecules (μ) are shown in (a)–(f). Time in a.u. $= 2.4189\times10^{-17}$ s, and all quantities in atomic units. Note the correlation between the increases in the magnitude of the excess electron binding energy (E_q) and the cluster dipole, as the nuclear configurations fluctuate.

the dimer and of the total (classical) energy [E_{cl}, Fig. 14(b)] we observe that the structural transitions from the low-dipole to high-dipole configurations are accompanied by a decrease in the magnitude of the interatomic interactions [compare Figs. 14(a), 14(b), and 14(f)]. We remark that the low-dipole configuration is the one closer to that of the neutral water dimer.[52(b)] Additional information about the internal nuclear motions within the negatively charged,

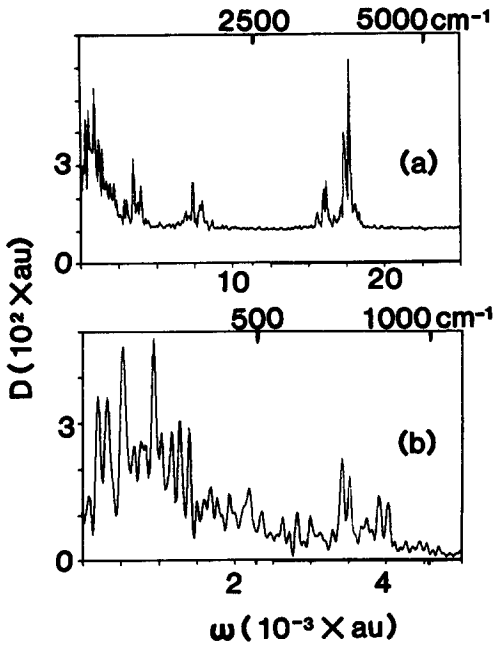

FIG. 15. Vibration density of states (D) spectra obtained from the velocity autocorrelation function generated via a 1.73×10^{-11} s classical molecular dynamics simulation of the neutral $(H_2O)_2^-$ cluster at 20 K. The full spectral range is shown in (a) and an expansion of the low-frequency range, corresponding to intermolecular motions, is shown in (b). The density of states and frequency are given in atomic units (the conversion to frequency in cm^{-1} is indicated at the top). Note in (a) the three spectral ranges discussed in the text.

as well as neutral, water dimers can be obtained from the nuclear frequencies which can be evaluated from the Fourier transform of the nuclear velocity correlation functions. The full vibrational density of state spectra obtained in this way for the neutral dimer is displayed in Fig. 15. In the spectrum shown in Fig. 15(a) three main frequency regimes can be distinguished: the high-frequency regime with $\omega > 3000$ cm^{-1} corresponding to intramolecular stretching vibrations, the medium frequency range with 1500 cm^{-1} $< \omega < 1700$ cm^{-1} corresponding to intramolecular bending vibration and a low-frequency regime with $\omega < 800$ cm^{-1} corresponding to intermolecular modes. An expanded view of the spectrum in the low-frequency regime is shown in Fig. 15(b). While we did not perform a detailed assignment of these spectra, the main features observed are in good agreement with the normal mode analysis of Reimers and Watts.[52(b)]

The neutral dimer spectra displayed in Fig. 15 were obtained using 9×10^4 classical time steps to generate a trajectory of duration 1.73×10^{-11} s. In Figs. 16 and 17 we show similar spectra for the negatively charged dimer. These spectra were generated as before using the nuclear velocities contained in the TDSCF trajectory. Here we use shorter trajectories both because of the much larger computational time involved and because the TDSCF trajectories can become numerically unstable for very long times. The duration of these trajectories was 1/6 of that used in Fig. 15. The resolution of the spectra in Figs. 16 and 17 is consequently consid-

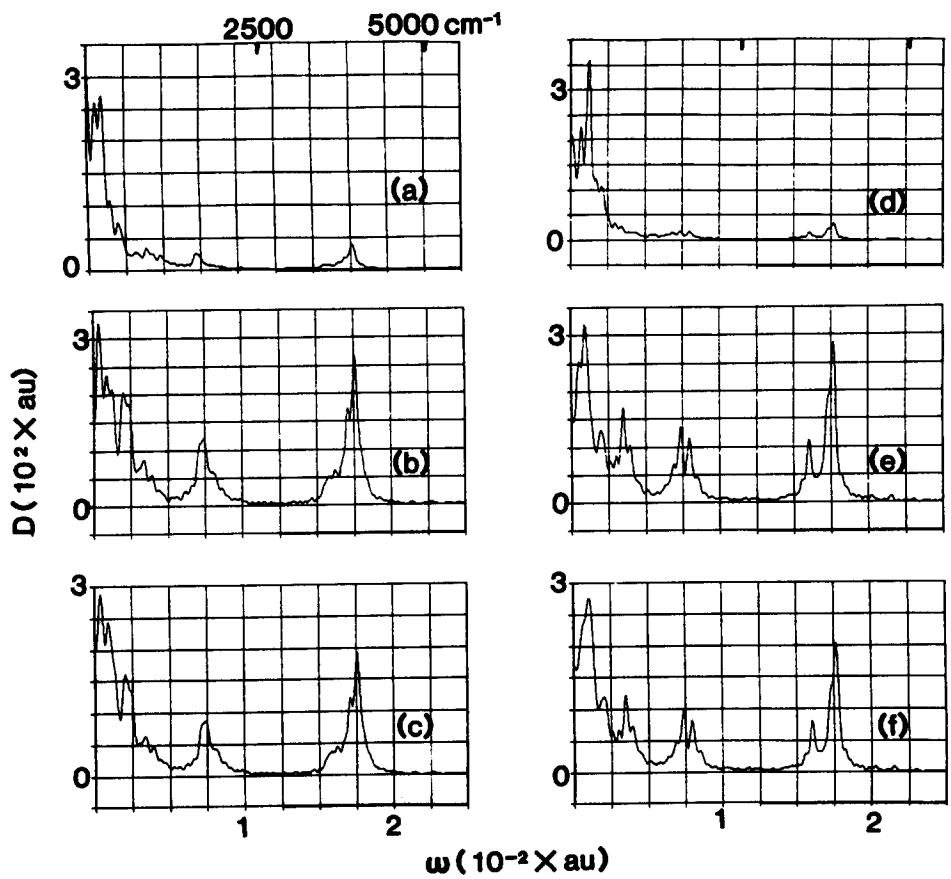

FIG. 16. Vibrational density of states (D) spectra obtained from the velocity autocorrelation functions (VAF) generated via TDSCF dynamics for $(H_2O)_2^-$ [shown in (a)–(c)], and via classical molecular dynamics for (H_2O_2) [shown in (d)–(f)], in simulation at 20 K whose length is 2.7×10^{-12} s. The full spectral range is shown. (a) and (d) are partial density of states derived from the VAF of the oxygens, (b) and (e) are the partial density of states for the hydrogens, and (c) and (f) are the total density of states. Density of states and frequency in atomic units (the conversions to frequency in cm^{-1} are indicated at the top).

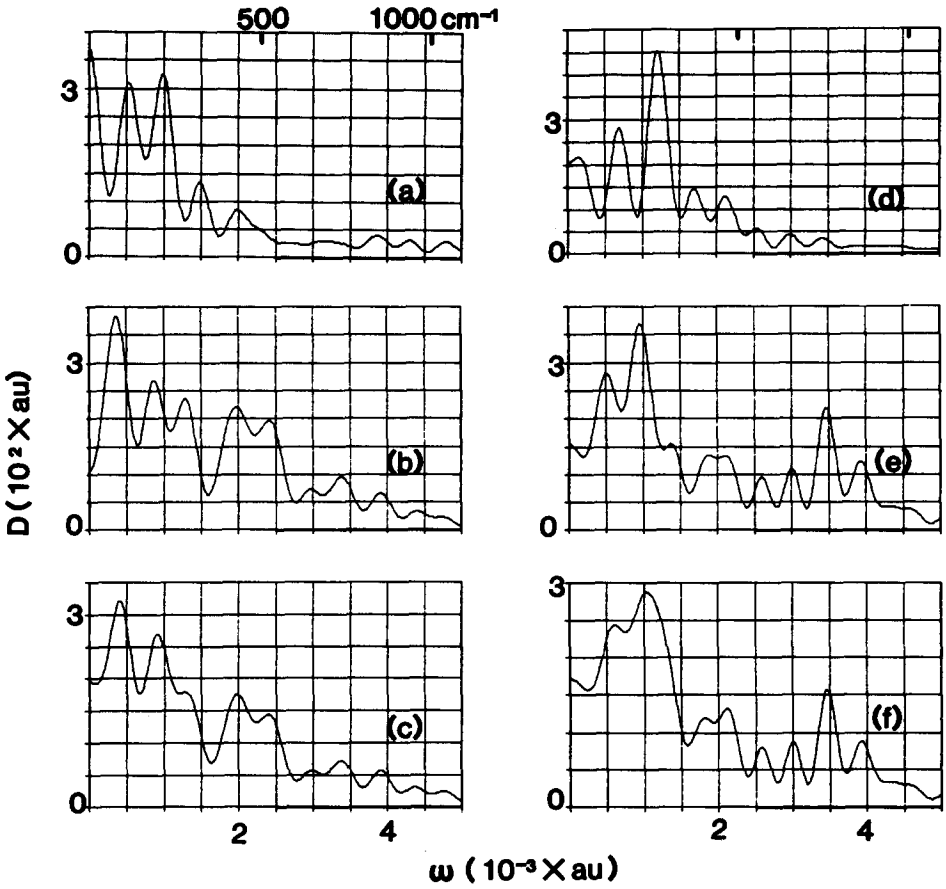

FIG. 17. Low-frequency region of the vibrational density of states. For further details see the caption to Fig. 16. Note the variations in the density of states upon electron attachment [compare (a)–(c) with (d)–(f)].

erably lower. To provide a better basis for comparison between the negatively charged and neutral cluster spectra we also include in these figures results for the neutral dimer with the same resolution (i.e., same trajectory length).

While the qualitative features in the neutral and the negatively charged dimer spectra are similar, comparison of the results shown in Figs. 16 and 17 reveal some important differences. First note that in the intramolecular frequency regime ($\omega > 1500\,\mathrm{cm}^{-1}$) the peaks associated with $(H_2O)_2^-$ are broader than the corresponding peaks in the neutral dimer. Several features which are distinctly resolved in Figs. 16(f) and 16(g) are not well resolved in Figs. 16(b) and 16(c). On the other hand, no observable shift between the spectra of the two clusters is seen (with our resolution) in this regime.

Second, the electron attachment has a substantial effect on the intermolecular low-frequency vibrations. Comparison of Figs. 17(a), 17(b), 17(c) and 17(f), 17(g), and 17(h) shows considerable frequency shifts, with most of the peaks in the $(H_2O)_2^-$ spectra shifting to the red while some modes in the region 400–500 cm^{-1} shift to the blue. Although detailed discussion of these effects is difficult because of the low resolution, it is reasonable to expect that such modes which strongly affect the total cluster molecular dipole will show a blue shift upon electron attachment because they are influenced by the contribution of the electron charge density to the force field. The in-plane intermolecular bend [mode $\nu_6(a')$ in Ref. 52(b)] with frequency 483 cm^{-1} in the neutral dimer may thus be the one responsible for the observed blue shift. Other modes, not directly associated with the cluster dipole will move to the red due to weakening in molecular bonding caused by the electron attachment, a similar effect to that seen in the $(NaCl)^-$ ion (Sec. IV).

VII. CONCLUSIONS

In this paper we have employed the fast Fourier transform (FFT) algorithm for solving the time-dependent Schrödinger equation and used it, in conjunction with the time-dependent self-consistent-field (TDSCF) approximation, to study the energetics, dynamical behavior, and spectroscopical properties of several negatively charged water clusters. First we have discussed and illustrated the use of the FFT method for obtaining eigenvalues and eigenfunctions of an electron moving in the potential of a static atomic configuration. We applied this method, using equilibrium cluster configurations calculated via quantum path-integral molecular dynamics (QUPID) simulations, to obtain energetic and spectroscopic information. For the large $(H_2O)_n^-$ clusters ($n \geqslant 32$) we have introduced and demonstrated the applicability of the adiabatic simulation method (ASM), in particular its ground-state dynamics (GSD) version. In this method the nuclear real-time dynamics evolves via classical mechanics, within the TDSCF approximation (i.e., under the influence of the quantum mechanically averaged potential), and the electron is restricted (by repeated use of imagi-

nary-time evolution) to the ground (or any other selected) state corresponding to the instantaneous nuclear configuration. Cluster size dependencies of ground- and excited-state dynamics and spectra were obtained in this way in an efficient manner. For the smallest negatively charged cluster, $(H_2O)_2^-$, we have used the TDSCF approximation to study the time evolution of the excess electron as well as the associated nuclear dynamics. The latter gave us, for the first time, an access to the vibrational spectrum of this negatively charged water cluster.

ACKNOWLEDGMENTS

This research was supported by U.S. DOE Grant No. FG05-86ER45234, by the U.S.–Israel Binational Science Foundation, and by the Israel Academy of Sciences and Humanities.

[1](a) U. Landman, D. Scharf, and J. Jortner, Phys. Rev. Lett. **54**, 1860 (1985); (b) D. Scharf, U. Landman, and J. Jortner, J. Chem. Phys. **87**, 2716 (1987).
[2](a) U. Landman, R. N. Barnett, C. L. Cleveland, D. Scharf, and J. Jortner, J. Phys. Chem. **91**, 4890 (1987); (b) R. N. Barnett, U. Landman, C. L. Cleveland, and J. Jortner, Phys. Rev. Lett. **59**, 811 (1987); (c) J. Chem. Phys. **88**, 4421 (1988); (d) **88**, 4429 (1988).
[3]A. Wallqvist, D. Thirumalai, and B. J. Berne, J. Chem. Phys. **85**, 1583 (1986).
[4]R. N. Barnett, U. Landman, C. L. Cleveland, N. R. Kestner, and J. Jortner, J. Chem. Phys. **88**, 6670 (1988); Chem. Phys. Lett. (in press).
[5]M. Parrinello and A. Rahman, J. Chem. Phys. **82**, 860 (1985).
[6]A. Selloni, P. Carenvali, R. Car, and M. Parrinello, Phys. Rev. Lett. **59**, 823 (1987).
[7]J. Schnitker and P. J. Rossky, J. Chem. Phys. **86**, 3462, 3471 (1987).
[8]J. Schnitker, K. Motakabbir, P. J. Rossky, and R. Friesher, Phys. Rev. Lett. **60**, 456 (1988).
[9]A. Wallqvist, D. Thirmulai, and B. J. Berne, J. Chem. Phys. **86**, 6404 (1987).
[10]C. D. Jonah, C. Romero, and A. Rahman, Chem. Phys. Lett. **123**, 209 (1986).
[11]D. E. Raedt, H. Sprik, and M. L. Klein, J. Chem. Phys. **80**, 5719 (1984); M. Sprik, R. W. Impy, and M. L. Klein, *ibid.* **83**, 5802 (1985).
[12]M. Sprik and M. L. Klein, J. Chem. Phys. **87**, 5987 (1987).
[13](a) D. F. Coker and B. J. Berne, J. Chem. Phys. (to be published); (b) D. F. Coker, D. Thirmulai, and B. J. Berne, *ibid.* **86**, 5689 (1987).
[14]D. Chandler, Y. Singh, and D. M. Richardson, J. Chem. Phys. **81**, 1975 (1984); A. L. Nichols III and D. Chandler, *ibid.* **84**, 398 (1986).
[15]D. M. Ceperley and E. L. Pollock, Phys. Rev. Lett. **56**, 351 (1986).
[16]F. F. Abraham and J. Q. Broughton, Phys. Rev. Lett. **59**, 64 (1987).
[17]D. M. Ceperley and M. H. Kalos, in *Monte Carlo Methods in Statistical Physics*, edited by K. Binder (Springer, Berlin, 1979).
[18]For a recent review see B. J. Berne and D. Thirumalai, Annu. Rev. Phys. Chem. **37**, 401 (1986), and references therein.
[19]D. Chandler and P. G. Wolynes, J. Chem. Phys. **74**, 4078 (1981).
[20]R. P. Feynman and A. R. Hibbs, *Quantum Mechanics and Path Integrals* (McGraw-Hill, New York, 1965); R. P. Feynman, *Statistical Mechanics* (Benjamin, Reading, 1972).
[21]R. Car and M. Parrinello, Phys. Rev. Lett. **55**, 2471 (1985).
[22]See Ref. 18.
[23]J. Chang and W. H. Miller, J. Chem. Phys. **87**, 1648 (1987).
[24]J. D. Doll, R. D. Colson, and D. L. Freeman, J. Chem. Phys. **87**, 1641 (1987).
[25]A. L. Nichols III and D. Chandler (preprint).
[26]M. D. Feit, J. A. Fleck, Jr., and A. Steiger, J. Comput. Phys. **47**, 412 (1982); M. D. Feit and J. A. Fleck, Jr., J. Chem. Phys. **78**, 301 (1983); **80**, 2578 (1984).
[27]D. Kosloff and R. Kosloff, J. Comput. Phys. **52**, 35 (1983).
[28]See review by R. Kosloff, J. Phys. Chem. (to be published).
[29]P. A. M. Dirac, Proc. Cambridge Philos. Soc. **26**, 376 (1930).
[30]A. D. Mclachlan, Mol. Phys. **7**, 139 (1964).
[31]For a review of the method see Ref. 28, and references therein.
[32]D. Kumamoto and R. Silbey, J. Chem. Phys. **75**, 5164 (1981).
[33]R. N. Barnett, U. Landman, and A. Nitzan, Phys. Rev. A (to be published).
[34]N. Makri and W. H. Miller, J. Chem. Phys. **87**, 5781 (1987).
[35]J. Kucar, H. D. Meyer, and L. S. Cederbaum, Chem. Phys. Lett. **140**, 525 (1987).
[36]R. H. Bisseling, R. Kosloff, R. B. Gerber, M. A. Ratner, L. Gibson, and C. Cerjan, J. Chem. Phys. **87**, 2760 (1987).
[37]Z. Kotler, R. Kosloff, and A. Nitzan (to be published).
[38]Z. Kotler, A. Nitzan, and R. Kosloff, in *Tunneling*, edited by J. Jortner and B. Pullman (Reidel, Boston, 1986), p. 193.
[39]B. Carmeli and H. Metiu, Chem. Phys. Lett. **133**, 543 (1987).
[40]R. Kosloff and C. Cerjan, J. Chem. Phys. **81**, 3722 (1984).
[41]J. R. Fox and H. C. Anderson, J. Phys. Chem. **88**, 4019 (1984). In our simulations we use the stochastic thermalization method for constant temperature simulations described by these authors, and the classical equations of motion are integrated using the velocity form of the Verlet algorithm.
[42]B. Helsing, A. Nitzan, and H. Metiu, Chem. Phys. Lett. **123**, 523 (1986).
[43]R. Kosloff and H. Talezer, Chem. Phys. Lett. **127**, 223 (1986).
[44]D. Scharf, U. Landman, and J. Jortner, Chem. Phys. Lett. **130**, 5504 (1986).
[45]T. M. Miller, D. G. Leopold, K. K. Murray, and W. C. Lineberger, J. Chem. Phys. **85**, 2368 (1986).
[46]R. J. Mawhorter, M. Fink, and J. G. Hartley, J. Chem. Phys. **83**, 4418 (1985).
[47]H. Haberland, H. G. Langosch, H. G. Schindler, and D. R. Worsnop, Surf. Sci. **156**, 157 (1985); H. Haberland, H. G. Schindler, and D. R. Worsnop, J. Chem. Phys. **81**, 3742 (1984).
[48]M. Knapp, O. Echt, D. Kreisle, and E. Recknagel, J. Chem. Phys. **85**, 636 (1986); J. Phys. Chem. **91**, 2601 (1987).
[49]J. V. Coe, D. R. Worsnop, and K. H. Bowen, J. Chem. Phys. **88**, 8014 (1988). The photoelectron measurements in this study are for $(H_2O)_n^-$ clusters in the range $11 \leqslant n \leqslant 20$. Recent measurements in this laboratory [K. Bowen (private communication)] provide evidence for a binding state of ~ 20 MeV in $(H_2O)_2^-$ in agreement with previous QUPID prediction [Ref. 2(a)] and our current results.
[50]H. Haberland, H. G. Schindler, and D. R. Worsnop, Ber. Bunsenges. Phys. Chem. **88**, 270 (1984).
[51]R. N. Barnett, U. Landman, C. L. Cleveland, and J. Jortner, Chem. Phys. Lett. (in press).
[52](a) J. R. Reimers, R. O. Watts, and M. L. Klein, Chem. Phys. **64**, 95 (1982); (b) J. R. Reimers and R. D. Watts, *ibid.* **85**, 83 (1984); see also Ref. 2(d). The RWK2-M model was used in our simulations.
[53]A. Hinchliffe, D. G. Bounds, M. L. Klein, I. R. McDonald, and R. Righini, J. Chem. Phys. **74**, 1211 (1981); "Model C" for the intermolecular potential was employed by us.
[54]D. J. Chipman, J. Phys. Chem. **82**, 1980 (1978).
[55]Recent calculations in which the ground-state dynamical evolution was followed while monitoring the time development of the *three* lowest excited states in $(H_2O)_{64}^-$ and $(H_2O)_{128}^-$ clusters corroborate these conclusions [R. N. Barnett, U. Landman, and A. Nitzan, J. Chem. Phys. (to be submitted)].
[56]A detailed examination of the energetics and dynamics of $(H_2O)_2^-$ is presented elsewhere: R. N. Barnett, U. Landman, N. R. Kestner, and A. Nitzan (in preparation).